Monthly Notices
of the
ROYAL ASTRONOMICAL SOCIETY

MNRAS **462,** 35–47 (2016) doi:10.1093/mnras/stw1612

A new method to measure galaxy bias by combining the density and weak lensing fields

Arnau Pujol,[1⋆] Chihway Chang,[2] Enrique Gaztañaga,[1] Adam Amara,[2] Alexandre Refregier,[2] David J. Bacon,[3] Jorge Carretero,[1,4] Francisco J. Castander,[1] Martin Crocce,[1] Pablo Fosalba,[1] Marc Manera[5] and Vinu Vikram[6,7]

[1]*Institut de Ciències de l'Espai (ICE, IEEC/CSIC), E-08193 Bellaterra, Barcelona, Spain*
[2]*Department of Physics, ETH Zurich, Wolfgang-Pauli-Strasse 16, CH-8093 Zurich, Switzerland*
[3]*Institute of Cosmology and Gravitation, University of Portsmouth, Dennis Sciama Building, Portsmouth PO1 3FX*
[4]*Institut de Física d'Altes Energies, Universitat Autònoma de Barcelona, E-08193 Bellaterra, Barcelona, Spain*
[5]*University College London, Gower Street, London WC1E 6BT*
[6]*Argonne National Laboratory, 9700 South Cass Avenue, Lemont, IL 60439, USA*
[7]*Department of Physics and Astronomy, University of Pennsylvania, Philadelphia, PA 19104, USA*

Accepted 2016 July 4. Received 2016 July 4; in original form 2016 January 2

ABSTRACT

We present a new method to measure redshift-dependent galaxy bias by combining information from the galaxy density field and the weak lensing field. This method is based on the work of Amara et al., who use the galaxy density field to construct a bias-weighted convergence field $\kappa_{\rm g}$. The main difference between Amara et al.'s work and our new implementation is that here we present another way to measure galaxy bias, using tomography instead of bias parametrizations. The correlation between $\kappa_{\rm g}$ and the true lensing field κ allows us to measure galaxy bias using different zero-lag correlations, such as $\langle\kappa_{\rm g}\kappa\rangle/\langle\kappa\kappa\rangle$ or $\langle\kappa_{\rm g}\kappa_{\rm g}\rangle/\langle\kappa_{\rm g}\kappa\rangle$. Our method measures the linear bias factor on linear scales, under the assumption of no stochasticity between galaxies and matter. We use the Marenostrum Institut de Ciències de l'Espai (MICE) simulation to measure the linear galaxy bias for a flux-limited sample ($i < 22.5$) in tomographic redshift bins using this method. This article is the first that studies the accuracy and systematic uncertainties associated with the implementation of the method and the regime in which it is consistent with the linear galaxy bias defined by projected two-point correlation functions (2PCF). We find that our method is consistent with a linear bias at the per cent level for scales larger than 30 arcmin, while non-linearities appear at smaller scales. This measurement is a good complement to other measurements of bias, since it does not depend strongly on σ_8 as do the 2PCF measurements. We will apply this method to the Dark Energy Survey Science Verification data in a follow-up article.

Key words: gravitational lensing: weak – surveys – large-scale structure of Universe.

1 INTRODUCTION

The formation and evolution of large-scale structure in the Universe is an important tool for cosmology studies. However, since most of the mass in the Universe is in the form of dark matter, which cannot be observed directly, we need to understand the connection between the observable Universe (galaxies and stars) and dark matter. In the ΛCDM paradigm, structures form in the initial density peaks, causing dark matter to collapse gravitationally and form virialized objects. Galaxies are expected to follow these gravitational potentials (e.g. White & Rees 1978) and because of this they are tracers of dark matter density peaks. The relation between galaxy and mass distributions can be described theoretically with the galaxy bias prescription (Kaiser 1984; Fry & Gaztanaga 1993; Bernardeau 1996; Mo & White 1996; Sheth & Tormen 1999; Manera, Sheth & Scoccimarro 2010; Manera & Gaztañaga 2011). The galaxy bias allows us to connect the distribution of galaxies with that of dark matter and a good knowledge of galaxy bias would be very important to improve the precision of our cosmological measurements (Eriksen & Gaztañaga 2015).

Many articles have studied halo and galaxy bias in simulations (Cole & Kaiser 1989; Kravtsov & Klypin 1999; Seljak & Warren 2004; Angulo, Baugh & Lacey 2008; Faltenbacher & White 2010;

⋆ E-mail: arnaupv@gmail.com

Tinker et al. 2010; Manera & Gaztañaga 2011; Paranjape et al. 2013; Pujol & Gaztañaga 2014; Zentner, Hearin & van den Bosch 2014; Carretero et al. 2015; Pujol et al. 2015) and the different ways to measure bias (Kravtsov & Klypin 1999; Bernardeau et al. 2002; Manera & Gaztañaga 2011; Roth & Porciani 2011; Pollack et al. 2014; Bel et al. 2015; Hoffmann et al. 2015). There are also several measurements of bias from observations, where usually dark matter clustering is assumed from a model or from simulations (Zehavi et al. 2011; Cacciato et al. 2012; Coupon et al. 2012; Jullo et al. 2012; Marín et al. 2013; Di Porto et al. 2014; Durkalec et al. 2015; Crocce et al. 2016). In most of these studies, however, the results depend strongly on assumptions regarding the cosmological parameters.

Gravitational lensing is the effect of light deflection due to perturbations in the gravitational potential arising from the mass distribution. It is a powerful tool to measure the mass distribution in the Universe, since the gravitational potential is affected by both baryonic and dark matter. Weak lensing refers to the statistical study of small distortions (around 1 per cent) in the shapes of a large number of galaxies due to this effect. Several recent, ongoing and future galaxy surveys aim to obtain large weak lensing data sets that will allow us to constrain cosmology better, including the Canada–France–Hawaii Telescope Lensing Survey (CFHTLenS: Heymans et al. 2012; Erben et al. 2013), the Hyper Suprime-Cam (HSC: Miyazaki et al. 2006), the Dark Energy Survey (DES: Dark Energy Survey Collaboration 2005; Flaugher 2005), the Kilo Degree Survey (KiDS: Kuijken et al. 2015), the Panoramic Survey Telescope and Rapid Response System (PanSTARRS: Kaiser et al. 2010), the Large Synoptic Survey Telescope (LSST: LSST Science Collaboration et al. 2009), *Euclid* (Laureijs et al. 2011), the Red Cluster Sequence Lensing Survey (RCSLenS: Hildebrandt et al. 2016) and the Wide-Field Infrared Survey Telescope (WFIRST: Green et al. 2012). From the shape of the galaxies, one can infer the lensing fields, which contain information regarding the projected matter distribution and can be used to generate 2D and 3D mass maps (Massey et al. 2007; Van Waerbeke et al. 2013; Vikram et al. 2015), statistically.

The combination of weak lensing and galaxy density information gives us a powerful handle for measuring galaxy bias. One way is by studying the cross-correlation between the aperture mass and number counts statistics, which are measurements of both dark matter and galaxy densities (Schneider 1998; van Waerbeke 1998). Hoekstra et al. (2002) use the Red-Sequence Cluster Survey (RCS) and the VIRMOS–DESCART survey to measure galaxy bias at $z \simeq 0.35$ from the zero lag cross-correlation between aperture mass and number counts. They also find a scale dependence of bias at scales below 100 arcmin. The same method has then been applied in more recent studies (Simon et al. 2007; Jullo et al. 2012; Mandelbaum et al. 2013; Buddendiek et al. 2016). Using a shear tomography analysis, Simon (2012) combined galaxy–galaxy lensing and galaxy clustering to constrain the 3D galaxy biasing parameters. Bias can also be obtained from the cross-correlation between lensing from the cosmic microwave background and galaxy densities (Giannantonio et al. 2016). Using another method, Amara et al. (2012, hereafter A12) used the COSMOS field to measure galaxy bias by reconstructing a bias-weighted shear map from the galaxy density field. Galaxy bias is estimated from the zero-lag cross-correlation between this bias-weighted shear map from the galaxy density field and the shear measured from galaxy shapes. Different parametrizations of bias are used to measure constant, non-linear and redshift-dependent bias.

In this article, we explore and extend the method from A12. We analyse whether the galaxy bias measured with our method is consistent with the linear bias obtained from the projected two-point correlation functions (2PCF). We find that our method can be affected by different parameters in the implementation, such as redshift binning, the redshift range used, angular scales, survey area and shot noise. Finally, we show how to measure the redshift-dependent galaxy bias by using tomographic redshift binning. Although this method is very similar to the one presented in A12, there are a few notable differences. First of all, A12 explore different smoothing schemes for the density field, while we explore pixelizing the maps and applying a top-hat filter. In A12, the lensing shear is estimated for each galaxy and the bias is measured from the predicted and measured shear of the galaxies, while we measure galaxy bias from the lensing maps generated. Finally, A12 fit different parametric biases using a wide range of redshifts for the galaxy density field, while here we implement a tomographic measurement, where we measure bias in redshift bins using the density field of galaxies in each particular bin. We apply this method to the DES Science Verification (SV) data in a second article (Chang et al. 2016, hereafter Paper II).

The article is organized as follows. In Section 2, we give an overview of the theory for our analysis. In Section 3, we present the method used to measure bias from the galaxy density and weak lensing fields and the numerical effects associated with the implementation of the method. In Section 4, we present the results of the different tests and the final measurement of redshift-dependent galaxy bias. Finally, we close in Section 5 with a discussion and conclusions.

2 THEORY

2.1 Galaxy bias

The distribution of galaxies traces that of dark matter and one of the common descriptions for this relation is galaxy bias, which relates the distribution of galaxies to that of dark matter. There are several ways to quantify galaxy bias (Bernardeau et al. 2002; Manera & Gaztañaga 2011; Roth & Porciani 2011; Bel et al. 2015; Hoffmann et al. 2015) and one of the most common is from the ratio of the 2PCF of galaxies and dark matter:

$$\xi_{\rm g}(r) = b^2(r)\xi(r), \tag{1}$$

where $b(r)$ is the galaxy bias and $\xi_{\rm g}(r)$ and $\xi(r)$ are the scale-dependent galaxy and matter 2PCF respectively, which are defined as

$$\xi_{\rm g}(r_{12}) = \langle \delta_{\rm g}(\boldsymbol{r_1})\delta_{\rm g}(\boldsymbol{r_2})\rangle, \qquad \xi(r_{12}) = \langle \delta(\boldsymbol{r_1})\delta(\boldsymbol{r_2})\rangle, \tag{2}$$

where $\delta_{\rm g} = (\rho_{\rm g} - \bar{\rho}_{\rm g})/\bar{\rho}_{\rm g}$ is the density fluctuation of galaxies ($\rho_{\rm g}$ is the galaxy number density) and $\delta = (\rho - \bar{\rho})/\bar{\rho}$ is the density fluctuation of dark matter (ρ is the dark matter density). As can be seen from this equation, galaxy bias generally depends on the scale r_{12} (defined as the distance between $\boldsymbol{r_1}$ and $\boldsymbol{r_2}$). However, it has been shown that, at sufficiently large scales in the linear bias regime, bias is constant (e.g. Manera & Gaztañaga 2011).

Bias can also be defined from the projected 2PCF:

$$\omega_{\rm g}(\theta) = b^2(\theta)\omega(\theta), \tag{3}$$

where $\omega_{\rm g}(\theta)$ and $\omega(\theta)$ refer to the projected 2PCF of galaxies and dark matter, respectively. This definition of bias will be used in the analysis in this article. In this case, the bias dependence is on separation angle θ instead of distance r.

In the local bias model approach (Fry & Gaztanaga 1993), the density field of galaxies is described as a function of its local dark

matter density, so that $\delta_g = F[\delta]$. We can express this relation as a Taylor series:

$$\delta_g = \epsilon + b_0 + b_1\delta + \frac{b_2}{2}\delta^2 + ... = \sum_{i=0}^{\infty} b_i(z)\delta^i + \epsilon, \quad (4)$$

where b_i are the coefficients of the Taylor expansion and ϵ represents the galaxy shot noise. The density contrasts δ_g and δ are smoothed to a certain scale by a window function, so the relation also depends on that physical scale. It also assumes no random scatter between δ_g and δ and ϵ is negligible for large smoothing scales. In the linear regime, $\delta \ll 1$, and, as $b_0 = 0$ because $\langle\delta_g\rangle = \langle\delta\rangle = 0$, the equation then becomes

$$\delta_g = b_1\delta. \quad (5)$$

According to Manera & Gaztañaga (2011), at large scales this definition of bias is consistent with the bias obtained from the 2PCF: for $r_{12} \gtrsim 40\,h^{-1}$ Mpc, b from equation (1) is approximately constant and consistent with b_1 from equation (5). This b_1 can then be measured from the different zero-lag correlations between δ_g and δ:

$$b_1 = \frac{\langle\delta_g\delta\rangle}{\langle\delta\delta\rangle}, \quad (6)$$

$$b_1 = \frac{\langle\delta_g\delta_g\rangle}{\langle\delta_g\delta\rangle}, \quad (7)$$

$$b_1 = \sqrt{\frac{\langle\delta_g\delta_g\rangle}{\langle\delta\delta\rangle}}. \quad (8)$$

Although these relations appear to measure the same parameter b_1, the results can be affected by the stochasticity in the relation between δ_g and δ, which can come from different effects, such as the stochasticity of bias and projection effects.

The galaxy bias from equations (6)–(8) depends on the smoothing scale used to measure δ and δ_g. For small scales, non-linearities in the relation between δ and δ_g appear and b_1 is no longer consistent with equation (3). Throughout the article, we will use these equations of bias for distributions projected on the sky. Then, the relations in this analysis will depend on angular distance (for equation 3) or smoothing angle (for equations 6–8). The relation between both scales of bias (smoothing and separation) is complex, since the smoothing of δ and δ_g on a scale Θ involves the correlation of all scales below Θ. However, in the linear and local regime, the bias is consistent with both scales and then all estimators can be compared.

2.2 Weak lensing

Weak gravitational lensing (see e.g. Bartelmann & Schneider 2001; Refregier 2003) measures the small changes of galaxy shapes and brightnesses due to the foreground mass distribution in the line of sight of the (source) galaxies. By studying this effect statistically, assuming that (lensed) galaxies are oriented randomly in the absence of lensing, one can infer the mass distribution in the foreground of these source galaxies. As the light distortion is affected by gravity, weak lensing allows us to measure the total mass distribution, including baryonic and dark matter.

The gravitational potential Φ of a given density distribution δ can be defined as

$$\nabla^2\Phi = \frac{3H_0^2\Omega_m}{2a}\delta, \quad (9)$$

where H_0 and Ω_m are the Hubble parameter and the matter density parameter today, respectively, and a is the scalefactor assuming a spatially flat Universe. Assuming general relativity and no anisotropic stress, the lensing potential for a given source at position $(\boldsymbol{\theta}, \chi_s)$ is given by the weighted line-of-sight projection of Φ:

$$\psi(\boldsymbol{\theta}, \chi_s) = 2\int_0^{\chi_s} \frac{\chi(\chi_s - \chi)}{\chi_s}\Phi(\boldsymbol{\theta}, \chi)\,d\chi, \quad (10)$$

where $\boldsymbol{\theta}$ is the angular position on the sky, χ refers to the comoving radius and χ_s is the comoving distance to the source. The distortion of source galaxy images can be described by the convergence κ and shear $\boldsymbol{\gamma}$ fields, which are defined as

$$\kappa = \frac{1}{2}\nabla^2\psi, \quad (11)$$

$$\boldsymbol{\gamma} = \gamma_1 + i\gamma_2 = \frac{1}{2}(\psi_{,11} - \psi_{,22}) + i\psi_{,12}, \quad (12)$$

where $\psi_{,ij} = \partial_i\partial_j\psi$. Focusing on the convergence field, combining equations (9), (10) and (11), we obtain

$$\kappa(\boldsymbol{\theta}, \chi_s) = \frac{3H_0^2\Omega_m}{2c^2}\int_0^{\chi_s}\frac{\chi(\chi_s - \chi)}{\chi_s}\frac{\delta(\boldsymbol{\theta}, \chi)}{a(\chi)}\,d\chi \equiv K[\delta]. \quad (13)$$

For simplicity, we define $q(\chi, \chi_s)$ as the lensing kernel of the integral of δ at χ with the source at χ_s:

$$q(\chi, \chi_s) = \frac{3H_0^2\Omega_m}{2c^2}\frac{\chi(\chi_s - \chi)}{\chi_s a(\chi)}, \quad (14)$$

so that

$$\kappa(\boldsymbol{\theta}, \chi) = \int_0^{\chi_s} q(\chi, \chi_s)\delta(\boldsymbol{\theta}, \chi)\,d\chi. \quad (15)$$

Note that κ corresponds to a weighted integral of the matter density fluctuations in the line of sight of the source galaxies.

3 METHOD

3.1 Simulation

For the analysis, we use the Marenostrum Institut de Ciències de l'Espai (MICE) Grand Challenge simulation (Crocce et al. 2015; Fosalba et al. 2015a,b), an N-body simulation of a ΛCDM cosmology with the following cosmological parameters: $\Omega_m = 0.25$, $\sigma_8 = 0.8$, $n_s = 0.95$, $\Omega_b = 0.044$, $\Omega_\Lambda = 0.75$, $h = 0.7$. It has a volume of $(3.072\,h^{-1}\,\mathrm{Gpc})^3$, with 4096^3 particles of mass $2.927 \times 10^{10}\,h^{-1}\,M_\odot$. The galaxy catalogue has been run according to a halo occupation distribution (HOD) and subhalo abundance matching (SHAM) prescriptions (Carretero et al. 2015). The parameters of the model have been fitted to reproduce clustering as a function of luminosity and colour from the Sloan Digital Sky Survey (Zehavi et al. 2011), as well as the luminosity function (Blanton et al. 2003, 2005a) and colour–magnitude diagrams (Blanton et al. 2005b). We use the MICECATv2 catalogue, an extension of the publicly available MICECATv1 catalogue.[1] The main difference between MICECATv1 and MICECATv2 is that MICECATv2 is complete for $i < 24$ from $z = 0.07$ to $z = 1.4$, while MICECATv1 is complete for an absolute magnitude of $M_r < -19$. The catalogue also contains the lensing quantities (γ_1, γ_2 and κ) at the position of each galaxy, calculated from the dark matter field with a resolution of $N_{side} = 8192$ in `healpix` (corresponding to a pixel size of

[1] http://cosmohub.pic.es/

∼0.43 arcmin). The lensing signal was computed using the Born approximation. As the lensing value assigned to a galaxy at a given 3D position is inherited from the corresponding pixel value of the dark matter lensing map in which that galaxy sits, the lensing quantities of the galaxies do not have shape noise.

3.2 Bias estimation

In this section, we introduce the method used to estimate galaxy bias from the lensing and density maps of galaxies in the MICE simulation. It consists of the construction of a template $\kappa_{\rm g}$ for the lensing map κ from the density distribution of the foreground galaxies, assuming equation (5). Substituting δ with $\delta_{\rm g}$ in equation (13) gives

$$\kappa_{\rm g}(\boldsymbol{\theta}) = \int_0^{\chi_{\rm s}} q(\chi, \chi_{\rm s})\delta_{\rm g}(\boldsymbol{\theta}, \chi)\,{\rm d}\chi. \tag{16}$$

When computing $\kappa_{\rm g}$ numerically, the integral is approximated by a sum over all lenses in the foreground of the sources:

$$\kappa_{\rm g}(\boldsymbol{\theta}) \simeq \sum_{i=1}^{N} \bar{q}^i \delta_{\rm g}^i(\boldsymbol{\theta})\Delta\chi^i, \tag{17}$$

where we have split the foreground galaxies into N redshift bins. $\Delta\chi^i$ refers to the redshift bin width of the ith bin in comoving coordinates, $\bar{q}^i$ is the mean lensing weight that corresponds to that redshift bin and $\delta_{\rm g}^i(\boldsymbol{\theta})$ is the galaxy density fluctuation in that redshift bin at position $\boldsymbol{\theta}$, where $\boldsymbol{\theta}$ now represents a pixel in the sky plane. $\delta_{\rm g}^i(\boldsymbol{\theta})$ is calculated through $\delta_{\rm g}^i(\boldsymbol{\theta}) = (\rho_{\rm g}^i(\boldsymbol{\theta}) - \bar{\rho}_{\rm g}^i)/\bar{\rho}_{\rm g}^i$, where $\rho_{\rm g}^i(\boldsymbol{\theta})$ is the density of galaxies projected on the line of sight in the ith redshift bin and position (pixel) $\boldsymbol{\theta}$ and $\bar{\rho}_{\rm g}^i$ is the mean density of galaxies in the redshift bin, calculated from all the galaxies inside the redshift bin. This measurement of $\bar{\rho}_{\rm g}^i$ gives a good estimate of the mean density if the redshift bin is wide enough. For narrow bins of redshift width below $\Delta z = 0.03$, a smoothing of $\bar{\rho}_{\rm g}^i$ as a function of redshift is needed to obtain a good estimate of the mean density, as discussed in Section 3.3. Notice that $\delta_{\rm g}^i(\boldsymbol{\theta})$ is calculated taking into account all galaxies inside the volume of the cell corresponding to each pixel and redshift bin. This means that it corresponds to a projection in redshift of the galaxy density field, weighted by the volume of the corresponding cell.

In Fig. 1, we show a schematic picture of the effects of equation (17). The dashed black line shows $q(z, z_{\rm s})$, defined from equation (14) in redshift coordinates, while the red solid line shows $\bar{q}^i$ in redshift bins of $\Delta z = 0.2$. We used $z_{\rm s} = 1.3$ for this figure. The blue shaded region represents $\delta_{\rm g}(z)$ for a random (just for the example) pixel in the sky using narrow redshift bins ($\Delta z = 0.05$). The blue solid line represents $\delta_{\rm g}^i$ for the redshift bins of $\Delta z = 0.2$. Equation (17) is then equivalent to the integral of the product of the blue and red solid lines.

Equation (17) is an approximation of equation (16), which assumes that the small fluctuations in redshift of $\delta_{\rm g}$ inside the bins do not affect the results. The mean of $q(\chi, \chi_{\rm s})\delta_{\rm g}(\chi)$ inside the bins can be approximated by the product of the means $\bar{q}^i\delta_{\rm g}^i(\boldsymbol{\theta})$. These approximations hold at large scales and when $q(\chi, \chi_{\rm s})$ and $\delta_{\rm g}(\chi)$ are not correlated.

We focus on the simplest case, where galaxy bias is linear, local and redshift-independent. In this case, we can estimate b from the following zero-lag correlations of κ and $\kappa_{\rm g}$:

$$b = \frac{\langle\kappa_{\rm g}\kappa\rangle}{\langle\kappa\kappa\rangle - \langle\kappa^N\kappa^N\rangle}, \tag{18}$$

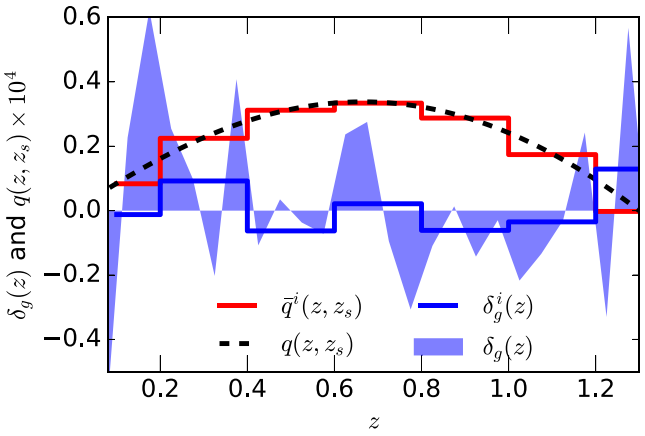

Figure 1. Schematic comparison of equations (16) and (17). The dashed black line shows $q(z, z_{\rm s})$, defined on a comoving scale in equation (14), for a fixed $z_{\rm s} = 1.3$, while the red solid line shows $\bar{q}^i$ from equation (17) in redshift bins of $\Delta z = 0.2$. The blue shaded region represents $\delta_{\rm g}(z)$ using narrow redshift bins ($\Delta z = 0.05$). The blue solid line represents $\delta_{\rm g}^i$ for redshift bins of $\Delta z = 0.2$. [A colour version of this figure is available in the online version.]

$$b = \frac{\langle\kappa_{\rm g}\kappa_{\rm g}\rangle - \langle\kappa_{\rm g}^N\kappa_{\rm g}^N\rangle}{\langle\kappa_{\rm g}\kappa\rangle}, \tag{19}$$

where κ^N and $\kappa_{\rm g}^N$ are the sampling and shot-noise correction factors obtained by randomizing the galaxy positions and re-calculating κ and $\kappa_{\rm g}$. κ is obtained from the mean κ of the galaxies in each pixel. This is affected by the number of source galaxies in the pixel, causing noise in $\langle\kappa\kappa\rangle$ that depends on the angular resolution used, reaching a 10 per cent error for a pixel size of 5 arcmin. This noise is cancelled by subtracting $\langle\kappa^N\kappa^N\rangle$. On the other hand, $\langle\kappa_{\rm g}\kappa_{\rm g}\rangle$ is affected by shot noise, causing an error that increases with angular resolution up to 20 per cent for a pixel size of 5 arcmin. This noise is cancelled by subtracting $\langle\kappa_{\rm g}^N\kappa_{\rm g}^N\rangle$. This correction assumes a Poisson distribution. To test how well this correction works for this method, we calculated $\langle\kappa_{\rm g}\kappa_{\rm g}\rangle - \langle\kappa_{\rm g}^N\kappa_{\rm g}^N\rangle$ using dark matter particles instead of galaxies and compared the results with the true $\langle\kappa\kappa\rangle$ maps from the simulation. We did this with different dilutions (from 1/70 to 1/700) of dark matter particles and we recover $\langle\kappa\kappa\rangle$ to better than 1 per cent independently of the dilution, indicating that shot-noise subtraction is appropriate.

Since the galaxies used from the MICE simulation do not have shape noise, the estimators in this analysis are not affected by shape noise. This is not the case in observations, where shape noise is the most important source of noise of this method and needs to be corrected. Moreover, in observations we do not have κ either; we need to obtain κ from $\boldsymbol{\gamma}$ and equations (11)–(12) in order to use these estimators. Notice that the galaxy bias obtained from equations (18)–(19) implies an average of bias as a function of redshift. This is because $\kappa_{\rm g}$ involves a redshift integral of $\delta_{\rm g} \sim b(z)\delta$ as specified in equation (16), so the final product is a redshift-averaged bias weighted by the lensing kernels that appear in equations (18)–(19). Later in this analysis, we use tomographic redshift bins, where we assume that bias does not change significantly inside the bin, and we measure bias in each of the redshift bins.

To measure the errors in b, we use the 'jack-knife' (JK) method. We divide the area into 16 subsamples. We evaluate b 16 times, each

time excluding a different subsample. The error in b is estimated from the standard deviation of these 16 measurements as

$$\sigma(b) \simeq \sqrt{\frac{N_{\rm JK}-1}{N_{\rm JK}}\sum_{i=1}^{N_{\rm JK}}(b_i-b)^2}, \tag{20}$$

where $N_{\rm JK}$ refers to the number of JK subsamples used, b_i is the bias measured by excluding the ith subsample and b is obtained from the average overall subsamples. We checked that the error is very similar if we use a different number of subsamples (between 9 and 100) instead of 16.

Note that we can also measure bias from the following cross-correlations:

$$b = \frac{\langle\gamma_{i,\rm g}\gamma_i\rangle}{\langle\gamma_i\gamma_i\rangle - \langle\gamma_i^N\gamma_i^N\rangle}, \tag{21}$$

$$b = \frac{\langle\gamma_{i,\rm g}\gamma_{i,\rm g}\rangle - \langle\gamma_{i,\rm g}^N\gamma_{i,\rm g}^N\rangle}{\langle\gamma_{i,\rm g}^N\gamma_i^N\rangle}, i = 1, 2. \tag{22}$$

As this is not the focus of the article and we can obtain κ from the simulation, we measure b from equations (18) and (19) in this study. However, in observations we measure the shape of the galaxies, which is directly related to γ_i. Because of this, applying this method to data requires a conversion from $\kappa_{\rm g}$ to $\gamma_{i,\rm g}$ or from γ_i to κ. These conversions imply other systematics, due to the finite area and the irregularities of the mask. The conversion from $\kappa_{\rm g}$ to $\gamma_{i,\rm g}$ can be affected by the shot noise in $\kappa_{\rm g}$, but this noise is less dominant than shape noise, which can affect the conversion from γ_i to κ. We address this issue in Paper II, where we use conversions based on Kaiser & Squires (1993, hereafter the KS method) to apply this method to DES SV data. Another aspect to take into account for data analysis is that, since shape noise is the main source of noise in the measurement, we like to avoid terms that involve variance of lensing quantities $\langle\kappa\kappa\rangle$ and $\langle\gamma_i\gamma_i\rangle$, since these terms are the most affected by shape noise.

3.3 Implementation

In Fig. 2, we illustrate our procedure. We used a ∼900 square degree area from the MICE simulation corresponding to $0^\circ < {\rm RA} < 30^\circ$ and $0^\circ < {\rm Dec.} < 30^\circ$. The top panel shows the convergence map κ of source galaxies located at $z \simeq 1$. The middle panel shows the constructed convergence template, $\kappa_{\rm g}$, derived via equation (17). Both maps have been generated by pixelizing the distributions in pixels of side 7 arcmin. Then, the pixelated maps have been smoothed using a circular top-hat filter of 50 arcmin radius from this pixelated map. The map obtained corresponds to an angular scale of 50 arcmin and the statistics do not depend on the scale of the previous pixelization (if the pixels are much smaller than the smoothing scale). We can see that $\kappa_{\rm g}$ is a biased version of κ at large scales. In the bottom panel, we show the scatter plot of κ versus $\kappa_{\rm g}$. The bias b shown in the plot is estimated via equation (18) and the error corresponds to the JK errors from equation (20). In red, we show a line crossing the origin and with slope corresponding to this estimated bias. We have checked that the b value derived from the zero-lag statistics is in agreement with a linear fit to the scatter plot at the 0.1 per cent level. This is an indication that we are in the linear regime, where we can assume equation (5).

We note that the expression for the bias from equations (18) and (19) assumes equation (5). However, κ is a projection of δ in the line of sight weighted by the lensing kernel, as well as $\kappa_{\rm g}$. Thus, the relation between κ and $\kappa_{\rm g}$ is a constant that comes from the

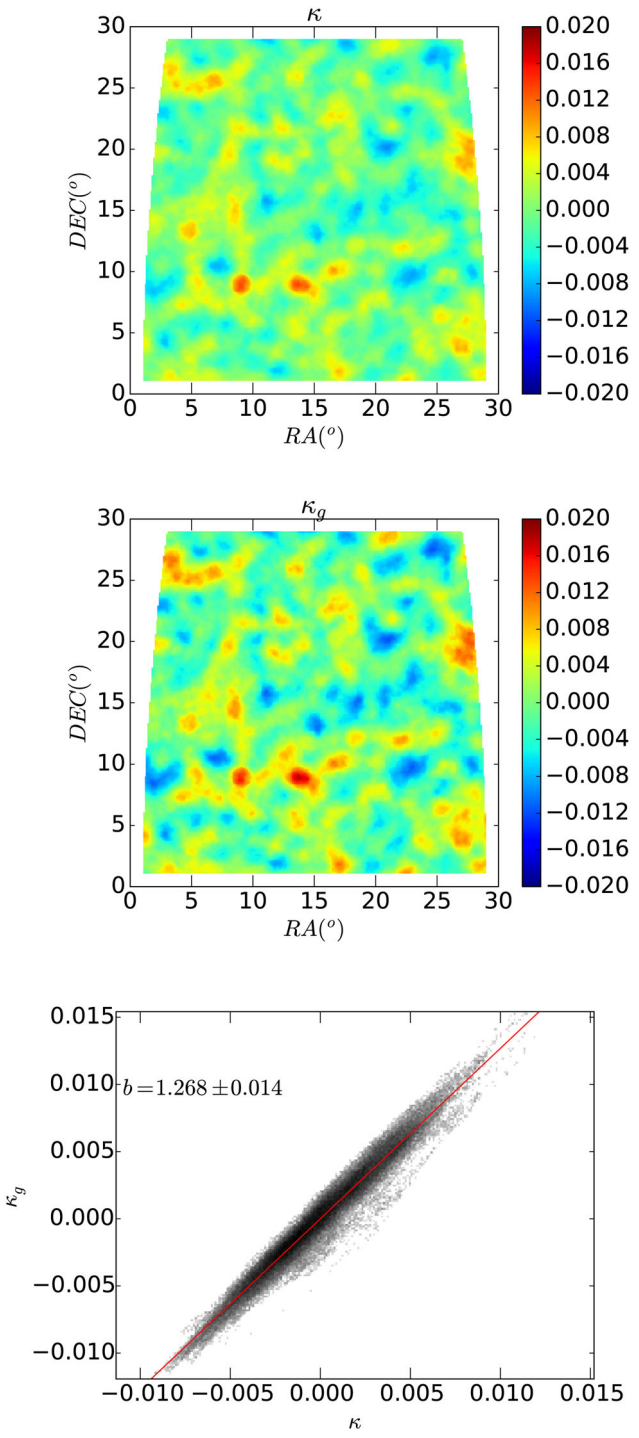

Figure 2. Comparison of κ versus $\kappa_{\rm g}$. The top panel shows the κ field from the source galaxies within $0.9 < z < 1.1$ and using a top-hat filter of 50 arcmin radius. The middle panel shows $\kappa_{\rm g}$ obtained from equation (17), using the same smoothing scheme. The bottom panel shows the comparison between $\kappa_{\rm g}$ and κ for the pixels of the maps, with the specified bias and error obtained. The red line corresponds to a line crossing the origin and its slope corresponds to b. It is consistent with the linear fit of the distribution of the points. [A colour version of this figure is available in the online version.]

redshift dependence of bias weighted by the redshift dependence of the lensing kernel. Hence, the bias obtained in this example is a weighted mean of galaxy bias as a function of redshift. However, we can take this dependence into account to measure bias at

different redshifts using tomography, as we explain in Section 3.4 below.

3.4 Redshift dependence

This method involves an integral (or a sum in practice) along the redshift direction and, because of this, the bias obtained is a weighted average of the redshift-dependent bias. However, we can estimate galaxy bias in a given redshift bin if we restrict the calculation to the foreground galaxies in that redshift bin, assuming that bias does not change significantly in the bin. If this is the case, we can measure the redshift-dependent bias using tomographic redshift bins.

Since $\kappa_{\rm g}$ is obtained from the contribution of all the galaxies in front of the sources, if we restrict the redshift range for the calculation of $\kappa_{\rm g}$, we need to renormalize the result by taking into account the contribution from the unused redshift range.

We define $\kappa_{\rm g}'$ as the construction of a partial $\kappa_{\rm g}$ using only the galaxies projected in a given redshift bin, so

$$\kappa_{\rm g}'(\boldsymbol{\theta}) = \int q(\chi, \chi_{\rm s}) p(\chi) \delta_{\rm g}(\boldsymbol{\theta}, \chi)\, {\rm d}\chi, \tag{23}$$

where $p(\chi)$ is the radial selection function, equal to 1 inside the bin $\chi_{\rm min} < \chi < \chi_{\rm max}$ and 0 outside. To simplify the notation, when the limits are not specified in the integral, the integral will go through the whole range between 0 and ∞. We assume that all the sources are located at $\chi_{\rm s}$ here and in the following and because of this we will not include the argument $\chi_{\rm s}$ in $\kappa_{\rm g}'(\theta)$ and other functions. Note that, as $p(\chi) = 0$ for all χ outside the bin, only the range $\chi_{\rm min} < \chi < \chi_{\rm max}$ contributes to the integral in equation (23) and $p(\chi)$ implies a projection inside the bin. In order to simplify the expression, if $q(\chi, \chi_{\rm s})$ is not correlated with $p(\chi)\delta_{\rm g}(\chi)$ inside the bin (which is the case, since $\delta_{\rm g}(\chi)$ decorrelates quickly in the redshift direction and hence the correlation is only important for very narrow bins), $q(\chi, \chi_{\rm s})$ can be described outside the integral as

$$\kappa_{\rm g}'(\boldsymbol{\theta}) \simeq \bar{q}'\Delta\chi \int p'(\chi)\delta_{\rm g}(\boldsymbol{\theta}, \chi)\, {\rm d}\chi = \bar{q}'\Delta\chi\bar{\delta}_{\rm g}', \tag{24}$$

with

$$\bar{q}' = \int_{\chi_{\rm min}}^{\chi_{\rm max}} \frac{q(\chi, \chi_{\rm s})}{\Delta\chi}\, {\rm d}\chi. \tag{25}$$

$\Delta\chi = \chi_{\rm max} - \chi_{\rm min}$ and now $p'(\chi)$ is the same selection function as $p(\chi)$ but normalized to 1, so $p'(\chi) = p(\chi)/\Delta\chi$.

With this definition, we measure the galaxy bias in this redshift bin, which we call b', from the following expressions:

$$b_1' = \frac{1}{f_1}\frac{\langle\kappa_{\rm g}'\kappa\rangle}{\langle\kappa\kappa\rangle - \langle\kappa^N\kappa^N\rangle}, \tag{26}$$

$$b_2' = \frac{1}{f_2}\frac{\langle\kappa_{\rm g}'\kappa_{\rm g}'\rangle - \langle\kappa_{\rm g}'^N\kappa_{\rm g}'^N\rangle}{\langle\kappa_{\rm g}'\kappa\rangle}, \tag{27}$$

where $\kappa_{\rm g}'^N$ is obtained by randomizing the positions of the galaxies in the redshift bin in order to correct for shot noise and f_1 and f_2 correspond to the following ratios:

$$f_1 = \frac{\langle\kappa'\kappa\rangle}{\langle\kappa\kappa\rangle} \tag{28}$$

and

$$f_2 = \frac{\langle\kappa'\kappa'\rangle}{\langle\kappa'\kappa\rangle}, \tag{29}$$

where κ' is defined as the contribution to κ of the dark matter field projected in the redshift bin used, so

$$\kappa'(\boldsymbol{\theta}) = \bar{q}'\Delta\chi \int p'(\chi)\delta(\boldsymbol{\theta}, \chi)\, {\rm d}\chi = \bar{q}'\Delta\chi\bar{\delta}'. \tag{30}$$

For our purpose, we are interested in the analytic expressions of $\langle\kappa'\kappa\rangle$, $\langle\kappa'\kappa'\rangle$ and $\langle\kappa\kappa\rangle$ to be able to use f_1 and f_2 to measure galaxy bias in tomographic redshift bins. According to the definitions, from equations (15) and (30) we can derive

$$\langle\kappa'\kappa(\theta)\rangle = \bar{q}'\Delta\chi' \int p'(\chi_1)\, {\rm d}\chi_1 \int_0^{\chi_{\rm s}} q(\chi_2)\xi(r_{12})\, {\rm d}\chi_2, \tag{31}$$

$$\langle\kappa'\kappa'(\theta)\rangle = (\bar{q}'\Delta\chi')^2 \int p'(\chi_1)\, {\rm d}\chi_1 \int p'(\chi_2)\xi(r_{12})\, {\rm d}\chi_2, \tag{32}$$

$$\langle\kappa\kappa(\theta)\rangle = \int_0^{\chi_{\rm s}} q(\chi_1)\, {\rm d}\chi_1 \int_0^{\chi_{\rm s}} q(\chi_2)\xi(r_{12})\, {\rm d}\chi_2, \tag{33}$$

with $r_{12}^2 = \chi_1^2 + \chi_2^2 + 2\chi_1\chi_2\cos\theta$, where $\xi(r_{12})$ is the 2PCF and θ is the angular separation between the two fields.

For the general case, the zero-lag correlation of two fields A and B at an angular scale Θ (corresponding to a radius R in the given redshift bin) is given by

$$\langle\kappa_A\kappa_B(\Theta)\rangle = \frac{4}{\pi R^4}\int_0^R r_1\, {\rm d}r_1 \int_0^R r_2\, {\rm d}r_2 \int_0^\pi \omega_{AB}(\theta)\, {\rm d}\eta, \tag{34}$$

where $\theta^2 = r_1^2 + r_2^2 - 2r_1r_2\cos\eta$, κ_A and κ_B can be κ, κ', $\kappa_{\rm g}$ or $\kappa_{\rm g}'$, η is the angular separation between the vectors $\boldsymbol{r_1}$ and $\boldsymbol{r_2}$ and $\omega(\theta)$ is a projected two-point angular correlation function of the two fields A and B, defined as

$$\omega_{AB}(\theta) = \int {\rm d}\chi_A \int q(\chi_A)q(\chi_B)p(\chi_A)p(\chi_B)\xi_{AB}(r)\, {\rm d}\chi_B, \tag{35}$$

where $p(\chi_{A,B})$ are the corresponding selection functions of the fields A and B and $\xi_{AB}(r)$ is the 3D two-point cross-correlation function, which in this case corresponds to the dark matter $\xi(r)$.

In order to be consistent with equations (24) and (30), when A (and also B) refers to the dark matter field limited in a redshift bin, we use the following expressions for the angular correlation functions:

$$\omega_{A'B}(\theta) = \bar{q}'\Delta\chi \int {\rm d}\chi_A \int {\rm d}\chi_B q(\chi_B)p'(\chi_A)p(\chi_B)\xi_{AB}(r) \tag{36}$$

$$\omega_{A'B'}(\theta) = \bar{q}'^2\Delta\chi^2 \int {\rm d}\chi_A \int p'(\chi_A)p'(\chi_B)\xi_{AB}(r)\, {\rm d}\chi_B, \tag{37}$$

where A' and B' refer to the cases where the fields A and B are restricted to the redshift bin and $\Delta\chi = \chi_{\rm max} - \chi_{\rm min}$ defines the redshift bin width of A' and B'.

Equations (28)–(29) can be predicted theoretically by assuming a cosmology. However, most of the cosmology dependence of the expression is cancelled out due to the ratios from f_1 and f_2, so the final factor is only weakly dependent on cosmology. In our case, we assume the cosmology of the MICE simulation. In Fig. 3, we show f_1 (top) and f_2 (bottom) for different cosmologies and theories, using an angular scale of 50 arcmin, normalized by the values corresponding to the MICE cosmology. Orange solid lines represent the MICE cosmology, predicted from the Eisenstein & Hu (1998) non-linear theory obtained using HALOFIT (Smith et al. 2003). The dashed green lines show the same but obtained from linear theory. We can see that the differences between using linear and non-linear theory are small compared with the final errors that we obtain from our method. We use the old version of HALOFIT for this prediction, which produces larger differences between the

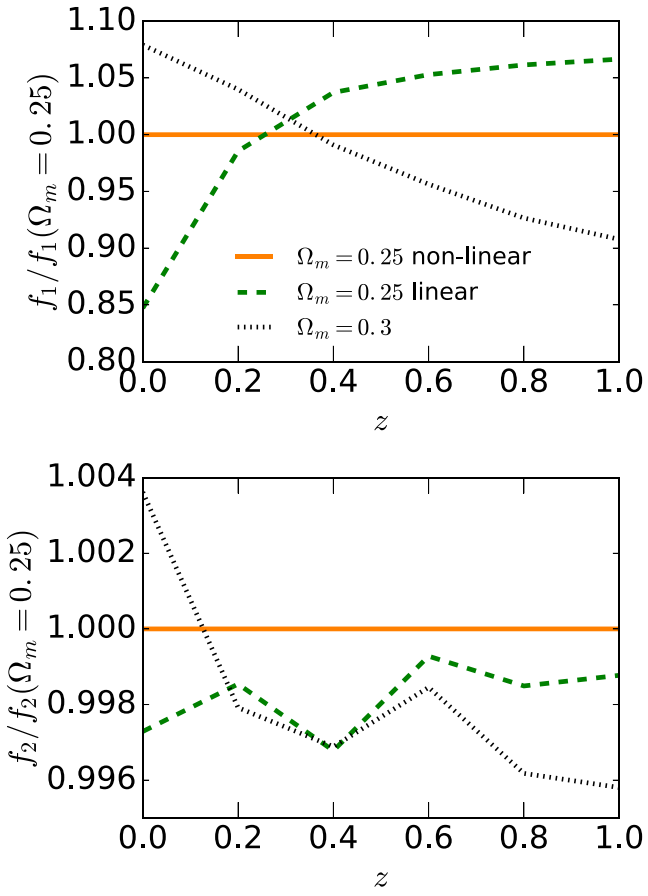

Figure 3. f_1 (top) and f_2 (bottom) for different theory cosmologies, normalized by the values from the MICE cosmology. Dotted lines are obtained for a cosmology with $\Omega_m = 0.3$, while the other two lines represent $\Omega_m = 0.25$. The orange solid line has been obtained using non-linear theory with HALOFIT (Smith et al. 2003), while the dashed green line has been obtained from linear theory using HALOFIT. [A colour version of this figure is available in the online version.]

MICE and theoretical linear power spectra (Fosalba et al. 2015a). On the other hand, to obtain the non-linear prediction, we computed the non-linearities at an intermediate redshift and extrapolated to other redshifts using linear growth, which causes a larger disagreement between the linear and non-linear predictions. Because of all this, the difference between the orange and dashed green lines may be interpreted as the upper bound of the disagreement between linear and non-linear theory.

Finally, in black dotted lines we show the predictions for the same cosmology but with $\Omega_m = 0.3$. We can see that the differences between both cosmologies are smaller than the errors in our bias estimation, even with the fact that the differences in Ω_m are very large and that Ω_m is the most sensitive parameter of these predictions. Hence, we can say that the cosmology dependence of this method is very weak.

Equations (28)–(29) describe the contribution of these zero-lag correlations of κ and κ' in a given redshift bin for the dark matter field. As the dark matter field has a bias of 1 by definition, using galaxies instead of the dark matter field to compute κ'_g instead of κ' in equations (28)–(29) would give $b'_{1,2} f_{1,2}$ instead of $f_{1,2}$, where $b'_{1,2}$ is the galaxy bias in the redshift bin used (assuming that the galaxy bias is constant inside the redshift bin). Then, to estimate the galaxy bias in these bins, we need to obtain the bias from equations (26)–(27).

3.5 Numerical effects and parameters

There are different parameters that can affect our implementation presented in Section 3.2. We have studied the regime in which our method is valid or consistent with the linear bias from equation (3) and the dependences when it is not valid. With this, we can either calibrate our results or restrict ourselves to the regimes where our bias measurement is carried out. Here, we describe the main numerical effects and our choice of parameters for our final implementation in Section 4.2.

3.5.1 Catalogue selection

We used an area of $0^\circ <$ RA, Dec. $< 30^\circ$. This is the same area we used for the fiducial bias measurements from equation (3), so that our comparison of both biases is not affected by differences in area or sample variance. This area is similar to that of the DES Y1 data, so this study can be seen as an estimation of the theoretical limitations of this method on DES Y1.

We apply a magnitude cut for the foreground galaxies of $i < 22.5$, to aid comparison in Paper II with measurements from the DES SV data (Crocce et al. 2016). However, other selections can be used for this method, such as selecting galaxies by colour or luminosity, in order to measure colour- and luminosity-dependent bias, which would give information about galaxy formation and evolution.

3.5.2 Redshift bin width

For the choice of Δz, we need to take into account two effects. On one hand, the use of wide redshift bins would mean losing information from small-scale fluctuations of δ_g in the line of sight, since we project the galaxies in the same bin to measure δ_g. We have seen that this produces a deviation in the value of galaxy bias that is larger than 5 per cent for $\Delta z > 0.2$ and can be larger than 10 per cent for $\Delta z > 0.3$. We explore this later in Section 4.1. We take this effect into account when we estimate the bias in tomographic bins at the end of the article. When we have photo-z errors, the redshift-binning effect is not as important as for the ideal case. If the photo-z errors dominate, dilution of small-scale fluctuations comes from the photo-z errors and redshift binning does not affect it much. We address the effects of photo-z errors in Paper II.

On the other hand, the use of narrow redshift bins requires a smoothing of the estimation of $\bar{\rho}_g(z)$. If we calculate $\bar{\rho}_g$ for each redshift bin alone, for narrow bins $\bar{\rho}_g(z)$ is affected by the structure fluctuation in each particular redshift bin and this causes a smoothing in the final estimation of δ_g. This happens because, when a redshift bin is dominated by an overdensity fluctuation, $\bar{\rho}_g(z)$ is overestimated and hence δ_g is underestimated. On the other hand, when the redshift bin is dominated by an underdensity, $\bar{\rho}_g(z)$ is underestimated and hence δ_g is overestimated. The final $\delta_g(z)$ is then smoothed, since all the values tend to be closer to zero due to the calculation of $\bar{\rho}_g(z)$. Some smoothing of $\bar{\rho}_g$ in redshift is needed to avoid this effect when using narrow bins. This is relevant for $\Delta z < 0.03$.

We use redshift bins of $\Delta z = 0.2$ for the foreground galaxies. In this analysis, we use the true redshift from the simulation, but in data this method would be also affected by photo-z errors. When photo-z errors are present, it is not worth using narrow redshift bins,

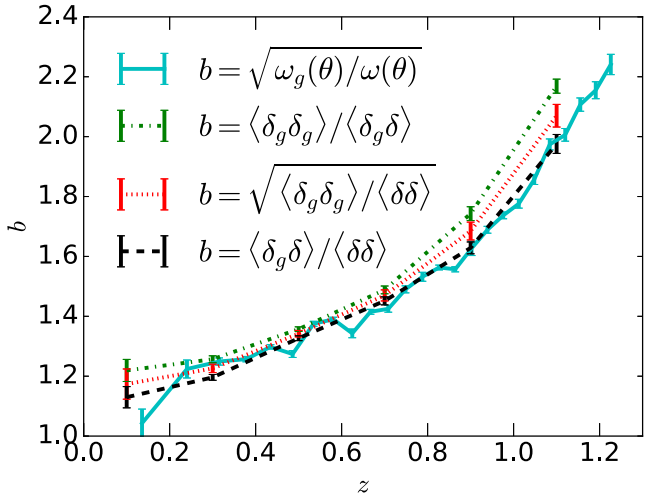

Figure 4. Comparison of different definitions of bias. The solid cyan line shows the bias as defined in equation (3). The dashed black, dash–dotted green and dotted red lines show the bias according to the different definitions from equations (6)–(8). [A colour version of this figure is available in the online version.]

since the uncertainty in redshift from photo-z errors dominates. We choose this redshift bin width for our estimation of bias in order to test how well we can recover galaxy bias with the redshift binning that is used in Paper II.

3.5.3 Angular scale

To generate maps, we pixelize the sky using a sinusoidal projection (which consists of redefining RA as (RA − 15) cos (Dec.) in order to obtain a symmetric map with pixels of equal area) with an angular resolution of 50 arcmin, so that the area of the pixels is (50 arcmin)^2. Then galaxies are projected in different redshift bins according to their true redshift.

The bias estimated from this method is not necessarily consistent with the bias from equation (3) at small scales. These two methods are only expected to agree at large scales, in the linear bias regime. Moreover, this method requires a projection in the line of sight, so that different scales (weighted differently according to the lensing kernel) are mixed for the same angular scale. However, we have seen that the bias is constant for angular scales $\Theta \gtrsim 30$ arcmin, meaning that linear scales are dominant in this regime. In Fig. 4, we show the agreement of galaxy bias between equations (3) and (6)–(8) when we use a pixel scale of 50 arcmin, as a visual example of this.

3.5.4 Smoothing

We do not apply any smoothing in the pixelized maps to estimate galaxy bias in this article. Exceptionally, for the maps in Fig. 2 we use pixels of 7 arcmin and apply a top-hat filter of 50 arcmin to smooth the maps. We do this only in this figure, in order to have better visibility of the structures in the maps and the shape of the area used. For the remainder of the analysis in this article, we use pixels of 50 arcmin and no apply smoothing kernel afterwards.

3.5.5 Edge effects

We use a limited area and we project the sky to obtain the maps. When we pixelize the map with a definite pixel scale, due to the projection and the shape of the area used, some of the pixels at the edges are partially affected by these edges. We exclude these pixels from the analysis.

When a smoothing kernel is applied to the pixelized map, the pixels that are close to the edges are also affected. We exclude those pixels with distance to the edges smaller than the smoothing radius.

3.5.6 Source redshift and redshift range

We estimate the κ field at $z \simeq 1.3$ by calculating the mean κ of the source galaxies with $1.2 < z < 1.4$ for each pixel. The redshift range used ensures we have enough density of galaxies to calculate κ correctly.

Theoretically, one should take into account the redshift distribution of the source galaxies, so that each galaxy contributes to κ_g with its position χ_s. However, approximating these galaxies to a plane in their mean position at $z \simeq 1.3$ causes less than a 1 per cent effect.

We use single redshift bins of $\Delta z = 0.2$ for the foreground galaxies in the range $0.2 < z < 1.2$ to estimate the bias in each of these bins. This produces a galaxy bias estimation of five points in the whole redshift range available (for this method) in the simulation.

4 RESULTS

4.1 Testing

In this study, we test our method against a fiducial galaxy bias. For this, we measure the angular 2PCF of matter and galaxies $\omega(\theta)$ and $\omega_g(\theta)$ in the simulation for different redshift bins, using the same area and galaxies as for our method. We also estimate the bias from the definitions in equations (6)–(8) in the same simulation, to study the consistency between the different bias definitions.

In Fig. 4, we compare different estimators of galaxy bias from the MICE simulation, using an area of $0^\circ < \mathrm{RA},\ \mathrm{Dec.} < 30^\circ$. The solid cyan line represents the bias definition from equation (3). We measure $\omega(\theta)$ and $\omega_g(\theta)$ as a function of angular scale and, to obtain the bias, we fit the ratio as constant between 6 and 60 arcmin. The angular correlation function involves different comoving scales for different redshifts and then fixing the same angular scales for the galaxy bias implies a mix of physical scales. However, for large enough scales, the bias is constant and is not affected by this. We have checked that bias does not change significantly at these scales and that using these scales to measure galaxy bias gives results consistent with using larger scales. The galaxy bias obtained from equations (6)–(8) is shown by dashed black, dotted red and dash–dotted green lines, as specified in the legend. This has been calculated in each redshift bin by pixelating δ and δ_g in pixels of area (50arcmin)^2 using redshift bins of $\Delta z = 0.2$. The agreement between the solid cyan and dashed black lines confirms that the linear bias from equation (3) is consistent with the local bias measure from equation (6) at these scales. On the other hand, the differences in the different expressions of equations (6)–(8) implies a stochasticity between δ_g and δ that affects our estimations of bias. We see that the same effect appears when using equation (40) to estimate galaxy bias; this can be explained by the projection effect due to redshift binning, as discussed below in Figs 5 and 6. We take this effect into account to estimate tomographic bias in Section 4.2.

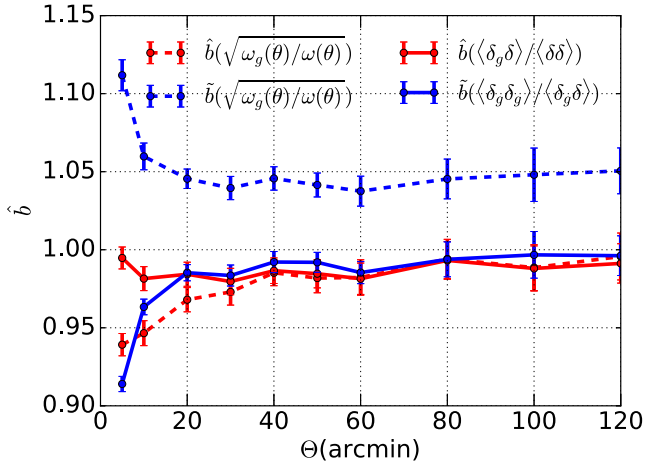

Figure 5. Bias from the zero-lag cross-correlations of κ and $\hat{\kappa}_{\rm g}$ as a function of angular scale, where $\hat{\kappa}_{\rm g}$ is an estimation of $\kappa_{\rm g}$ normalized by the redshift-dependent bias from different estimators, as in equations (38)–(40). The dashed red line shows $\hat{b}(\sqrt{\omega_{\rm g}(\theta)/\omega(\theta)})$. The solid red line shows the same, but obtaining $\hat{\kappa}_{\rm g}$ from the bias from equation (6) to yield $\hat{b}(\langle\delta_{\rm g}\delta\rangle/\langle\delta\delta\rangle)$. The dashed blue line shows $\tilde{b}(\sqrt{\omega_{\rm g}(\theta)/\omega(\theta)})$. The solid blue line shows the same $\tilde{b}$, but normalizing $\hat{\kappa}_{\rm g}$ from equation (7) to obtain $\tilde{b}(\langle\delta_{\rm g}\delta_{\rm g}\rangle/\langle\delta_{\rm g}\delta\rangle)$. [A colour version of this figure is available in the online version.]

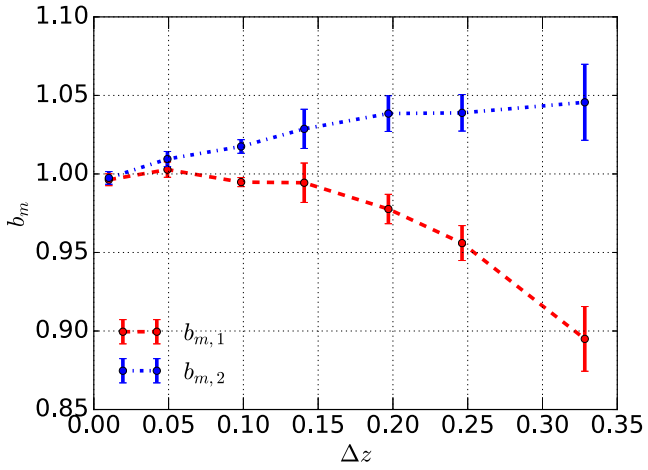

Figure 6. $b_{m,1}$ and $b_{\rm m,2}$, defined in equations (42) and (43), as a function of the redshift bin width used, Δz, for the two estimators. [A colour version of this figure is available in the online version.]

The idea of the following analysis is to test how the calculations for this method deviate from the expected estimation of linear bias using different angular scales and binning. For testing purposes, we construct here the bias-corrected $\kappa_{\rm g}$ map, $\hat{\kappa}_{\rm g}$, defined as

$$\hat{\kappa}_{\rm g}(b,\boldsymbol{\theta}) = \sum_{i=1}^{N} q^i \frac{\delta_{\rm g}^i(\boldsymbol{\theta})}{b^i}\Delta\chi^i, \tag{38}$$

where b^i corresponds to the linear bias measured in N bins that can be obtained from equations (3) or (6)–(8). In analogy with equations (18) and (19), we can calculate the corresponding normalized bias between the $\hat{\kappa}_{\rm g}$ and κ fields:

$$\hat{b}(b) = \frac{\langle\hat{\kappa}_{\rm g}(b)\kappa\rangle}{\langle\kappa\kappa\rangle - \langle\kappa^N\kappa^N\rangle}, \tag{39}$$

$$\tilde{b}(b) = \frac{\langle\hat{\kappa}_{\rm g}(b)\hat{\kappa}_{\rm g}(b)\rangle - \langle\kappa_{\rm g}^N\kappa_{\rm g}^N\rangle}{\langle\hat{\kappa}_{\rm g}(b)\kappa\rangle}. \tag{40}$$

Note that $\hat{b}$ and $\tilde{b}$ depend on the bias b used to obtain $\hat{\kappa}_{\rm g}$. Under this definition, $\hat{b}=1$ and $\tilde{b}=1$ suggest that this method is consistent with measuring the linear bias b.

Fig. 5 shows how the estimators $\hat{b}$ and $\tilde{b}$ change as a function of the angular scale, defined by the pixel scale, for different estimators of bias used to obtain $\hat{\kappa}_{\rm g}$. For the dashed red and blue lines, we used $b(z)$ from equation (3) to obtain $\hat{\kappa}_{\rm g}$ for our estimation of $\hat{b}(\sqrt{\omega_{\rm g}(\theta)/\omega(\theta)})$ and $\tilde{b}(\sqrt{\omega_{\rm g}(\theta)/\omega(\theta)})$, respectively. We can see that the measurements are constant for $\Theta > 30$ arcmin, meaning that we are in the linear regime in these scales. However, there is a 5 per cent difference between the two estimators at large scales (at small scales, non-linearities appear and the difference is larger). This can be interpreted using Fig. 4, where we see that the estimators from equations (6) (represented as a dashed black line) and (7) (represented as a dash–dotted green line) are slightly different. In fact, $\hat{b}$ is indirectly measuring equation (6), which is consistent with bias from equation (3) (at the 1 per cent level), while $\tilde{b}$ is indirectly measuring equation (7), which is slightly higher than the bias from equation (3). If we use equation (6) for the calculation of $\hat{\kappa}_{\rm g}$ to obtain $\hat{b}(\langle\delta_{\rm g}\delta\rangle/\langle\delta\delta\rangle)$ (shown by the solid red line) and equation (7) for the calculation of $\hat{\kappa}_{\rm g}$ to obtain $\tilde{b}(\langle\delta_{\rm g}\delta_{\rm g}\rangle/\langle\delta_{\rm g}\delta\rangle)$ (shown by the solid blue line), then both estimations are consistent, as expected. As in Fig. 4, the difference between both estimators coming from $\hat{b}(\sqrt{\omega_{\rm g}(\theta)/\omega(\theta)})$ and $\tilde{b}(\sqrt{\omega_{\rm g}(\theta)/\omega(\theta)})$ can be seen as an indication (and a measurement) of the stochasticity in the relation between $\delta_{\rm g}$ and δ, giving a factor of 5 per cent.

In order to go deeper into the analysis of these effects and see whether these differences between both estimators come from the intrinsic relation between $\delta_{\rm g}$ and δ or from numerical systematics, we constructed the following template $\kappa_{\rm m}$:

$$\kappa_{\rm m}(\boldsymbol{\theta}) = \sum_{i=1}^{N} q^i\delta^i(\boldsymbol{\theta})\Delta\chi^i, \tag{41}$$

which corresponds to the same exact calculation as in equation (17) for $\kappa_{\rm g}$, but using dark matter particles instead of galaxies. This field $\kappa_{\rm m}$ is expected to reproduce κ from the Born approximation consistently, except for numerical differences between the method and the way the original κ is obtained; thesebasically come from the redshift binning and projection discussed below equation (17). In order to avoid noise in the κ map, we use $\kappa_{\rm T}$, defined as the true map obtained directly from the high-resolution map of the simulation (see Gaztanaga & Bernardeau 1998; Fosalba et al. 2008, 2015b) and we calculate the bias of these two estimators of κ as

$$b_{\rm m,1} = \frac{\langle\kappa_{\rm m}\kappa_{\rm T}\rangle}{\langle\kappa_{\rm T}\kappa_{\rm T}\rangle}, \tag{42}$$

$$b_{\rm m,2} = \frac{\langle\kappa_{\rm m}\kappa_{\rm m}\rangle - \langle\kappa_{\rm m}^N\kappa_{\rm m}^N\rangle}{\langle\kappa_{\rm m}\kappa_{\rm T}\rangle}, \tag{43}$$

which should give $b_{\rm m,\,1,\,2}=1$ if there are no numerical systematics.

We have found that $b_{\rm m,\,1,\,2}$ behaves as $\hat{b}$ and $\tilde{b}$ in our tests, meaning that the differences between the different estimators can be seen as a measurement of the numerical effects on the method. In fact, we have found that the differences come mainly from the projection effect in the redshift bins, as shown in Fig. 6. Here we show $b_{\rm m,\,1}$ and $b_{\rm m,\,2}$ as a function of the redshift bin width, Δz, used to obtain $\kappa_{\rm m}$. We use a pixel scale of 50 arcmin, a source redshift

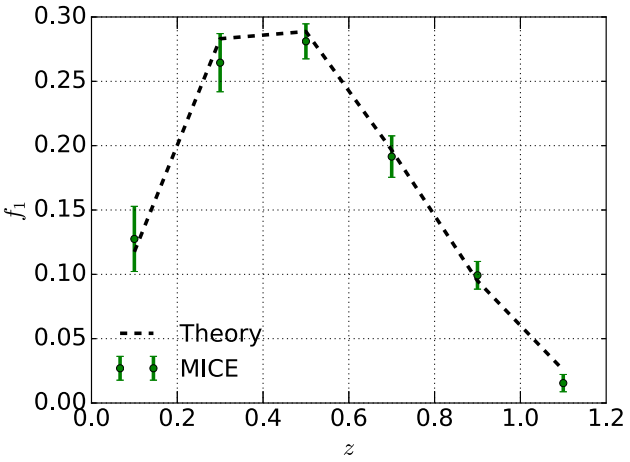

Figure 7. Comparison of f_1 from the simulation (green points) and the theory prediction (dashed black line). Each value has been obtained using redshift bins of $\Delta z = 0.2$ to calculate κ' and a source redshift $z_s = 1.3$. [A colour version of this figure is available in the online version.]

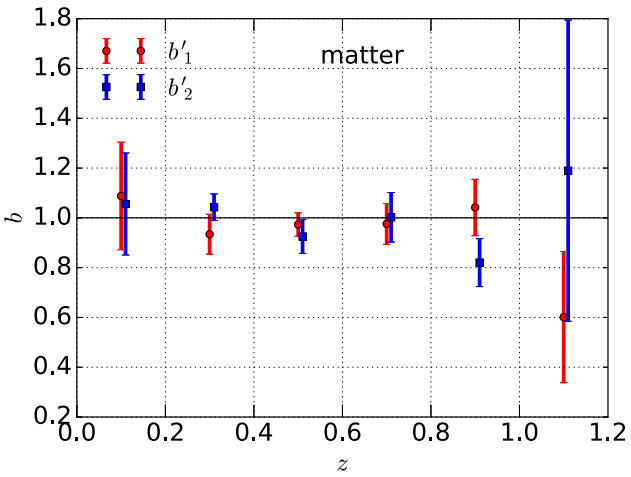

Figure 8. Tomographic bias of dark matter in the MICE simulation, using the two bias estimators from equations (26) and (27). We use tomographic redshift bins of $\Delta z = 0.2$ and a source redshift $z_s = 1.3$. [A colour version of this figure is available in the online version.]

of $z_s = 1$ and all dark matter particles (diluted with respect to the total number of particles, but this does not affect the result) within $z < 1$. We see that the two estimators agree when we use narrow redshift bins, but the difference between both increases with Δz. For $\Delta z = 0.2$, the difference is the 5 per cent that we see in Fig. 5 for the galaxies. This test measures the redshift binning and the projection impacts on this method and can also be used to calibrate the measurements. In fact, f_1 and f_2 can be used to take into account these projections, specified by the selection function $p'(\chi)$, and the redshift binning. In the case of Figs 5 and 6, however, we use the entire redshift range in the foreground of the sources and we have not corrected by f_1 and f_2. In the case of Fig. 5, this effect is visible for $\hat{b}(\sqrt{\omega_g(\theta)/\omega(\theta)})$ and $\tilde{b}(\sqrt{\omega_g(\theta)/\omega(\theta)})$. However, for $\hat{b}(\langle\delta_g\delta\rangle/\langle\delta\delta\rangle)$ and $\tilde{b}(\langle\delta_g\delta_g\rangle/\langle\delta_g\delta\rangle)$ the projection effect is compensated because we use the same redshift binning (and then the projection effects are the same and compensate) to obtain $\langle\delta_g\delta\rangle/\langle\delta\delta\rangle$, $\langle\delta_g\delta_g\rangle/\langle\delta_g\delta\rangle$, $\hat{b}$ and $\tilde{b}$. In the next section, we will apply the f_1 and f_2 corrections to the tomographic estimations.

4.2 Redshift dependence of bias

In Fig. 7 we show a comparison between the theoretical predictions (in dashed black lines) of f_1 and the measurements in the MICE simulation (in green points), for six different redshift bins of $\Delta z = 0.2$, using a redshift for the sources of $z_s = 1.3$. We see good agreement between theory and simulations. The redshift dependence of f_1 comes from the contributions of the lensing kernel, which causes the amplitude of f_1 to be higher at intermediate redshifts, but is also affected by the binning (which implies a projection of $p'(\chi)\delta(\chi)$ inside the bin) and the correlation functions from equations (31)–(33) (which has a contribution coming from the correlation between the dark matter distribution inside and outside the bin). The redshift dependence of the amplitude of f_1 reflects the contribution to $\hat{b}$ of each of these redshift bins.

Equations (26) and (27) provide a tool that can be used for tomographic measurements of galaxy bias, since we can estimate the bias using different redshift bins of the foreground galaxies if we take this correction into account. That is, we can measure $b'_{1,2}$ for a given redshift by calculating κ'_g in that bin and using equations (26) and (27).

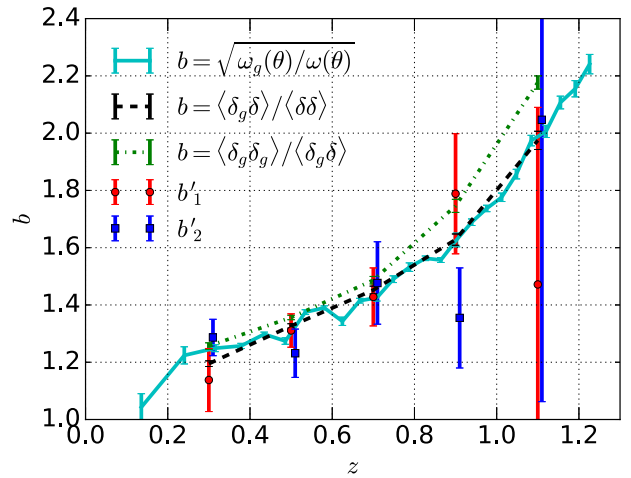

Figure 9. Redshift-dependent bias estimated from our method, shown in red and blue points as specified in the legend and equations (26)–(27). For this, we used tomographic redshift bins of $\Delta z = 0.2$ and a source redshift $z_s = 1.3$. The solid cyan line shows the linear bias from equation (3), fitting the bias as constant between 6 and 60 arcmin. The dashed black line shows the bias estimated from $\langle\delta_g\delta\rangle/\langle\delta\delta\rangle$, using the same redshift bins of $\Delta z = 0.2$. The dash–dotted green line shows the bias estimated from $\langle\delta_g\delta_g\rangle/\langle\delta_g\delta\rangle$ in the same redshift bins. [A colour version of this figure is available in the online version.]

In Fig. 8, we show a test where we obtain the tomographic bias of dark matter from the MICE simulations using this method. For this, we use κ' instead of κ'_g in equations (26) and (27) in order to estimate the bias of matter. By construction, the results should be consistent with 1. Our results are consistent, meaning that our method estimates tomographic bias correctly. We observe that the errors in these estimations are smaller at intermediate redshifts and larger at the extremes. This is due to the redshift dependence of f_1, which optimizes the signal for a high amplitude of f_1. When f_1 is small, the estimation of bias becomes noisier.

Fig. 9 shows the estimation of the tomographic galaxy bias using different redshift bins of $\Delta z = 0.2$ for both estimators from

equations (26) and (27), represented as red and blue points as specified in the legend. We compare them with the fiducial bias from equations (3), (6) and (7), shown as solid cyan, dashed black and dash–dotted green lines, respectively. We see that the method we present in this article gives consistent results with linear bias. There are some slight differences for the estimator from equation (7), which, as mentioned above, is due to the effects of projection and binning. However, this effect is not shown by the tomographic bias obtained from our method, because we take this effect into account in the factors f_1 and f_2. Note also that the two methods, represented by the red and blue points, give very similar results (apart from the fourth bin).

We can see that the errors are very large for the highest redshift bin. This is due to the fact that, due to the lensing kernel, f_1 and f_2 are very small and then the measurements in this bin are very sensitive to small changes. The best error bars appear where the lensing kernel is higher, so the potential of this method is optimal in the maximum of the lensing kernel. Hence, different source redshifts might be combined in order to optimize the analysis for all redshifts. In Paper II, we combine the results using multiple redshift bins for the source galaxies and fit the galaxy bias from the combination of these measurements, using both $\kappa_{\rm g}$ and $\gamma_{\rm g}$ and performing a full covariance analysis. In this article we do not apply any fit, since we measure bias directly from equations (26) and (27) using a fixed source redshift bin.

In this article we show this method for the most idealistic case. However, when applying this method to observations, other effects appear to be relevant. First of all, we cannot measure κ directly from observations and then we need to convert γ to κ or $\kappa_{\rm g}$ to $\gamma_{\rm g}$ to measure bias from equations (18) and (19) or (21) and (22). This involves some edge effects when these conversions are applied to a finite area. Moreover, foreground galaxy incompleteness, photo-z estimation, shape noise, mask and intrinsic alignments can affect our results in observations. We address these effects in Paper II.

5 DISCUSSION AND CONCLUSIONS

In this article, we explore a new method to measure galaxy bias from the combination of galaxy density and weak lensing fields. This method is based on A12, who use the galaxy density field to construct a bias-weighted convergence map $\kappa_{\rm g}$ in the COSMOS field. They measure different parametrizations of galaxy bias from the zero-lag correlations of the galaxy shear and a reconstruction of the shear from the galaxy density field. In this article, we present a new way to measure tomographic bias from the zero-lag correlations between the lensing maps and a reconstruction of the lensing maps from the galaxy density field. We also study the robustness and the systematics of this method for the first time.

The implementation of this model is as follows. We construct a template of the convergence field $\kappa_{\rm g}$ at the source redshift by integrating the density field of the foreground galaxies in the line of sight weighted by the corresponding lensing kernel, as specified in equation (16). We do this for tomographic bins in the lens distribution to obtain $\kappa'_{\rm g}$ as defined in equation (24). We then compare this with estimates of the matter convergence map κ associated with the same galaxies in the source redshift bin. We measure galaxy bias from the zero-lag cross-correlations between κ and $\kappa'_{\rm g}$, as in equations (26) and (27). Instead of using the zero-lag cross-correlation, we could also use the two-point cross-correlation function. We will apply this for DES Y1 data in a follow-up article.

We use the MICE simulations to study the consistency of our method by comparing our results with a fiducial galaxy bias measurement on linear scales. This is obtained from the ratio between the projected 2PCF of galaxies and dark matter as a function of redshift (see equation 3) and by fitting a constant galaxy bias between 6 and 60 arcmin. We also study the local bias from equations (6)–(8), making use of the dark matter field of the simulation. With these comparisons, we study the systematics of the method and the regimes in which it is consistent with linear bias.

There are different systematic effects and numerical dependences of the method that need to be taken into account for a correct measurement of linear bias. First of all, the method is sensitive to the redshift bin width used in the construction of $\kappa_{\rm g}$ and $\kappa'_{\rm g}$, which has an impact on galaxy bias estimators due to the projection effects of the density fields. This causes differences in the values obtained for the different estimators, which can be larger than 5 per cent for $\Delta z > 0.2$ and larger than 10 per cent for $\Delta z > 0.3$. This has to be taken into account and corrected when measuring $\kappa_{\rm g}$ and $\kappa'_{\rm g}$ in wide redshift bins, in order to obtain the correct linear bias. On the other hand, assuming that all the source galaxies (selected in a redshift bin of $\Delta z > 0.2$) are in a plane has an insignificant impact on the results. Secondly, the angular scale of the field can be affected by non-linearities for small enough scales. We find that the measurements are consistent with linear bias for angular scales of $\Theta > 30$ arcmin, where the bias is constant. Sampling and discreteness noise are also important and need to be taken into account (see equations (18) and (19)). Finally, we need to exclude from the analysis those pixels that are affected by the edges of the area used.

The true κ field comes from the contribution of the entire mass distribution in the whole redshift range below the source redshift. Then, if we only use a fraction of this redshift range to calculate $\kappa_{\rm g}$, the correlation between κ and $\kappa_{\rm g}$ is lower, due to the fact that we are not comparing the same redshift ranges. A correction must then be applied to our estimators if we only use the foreground galaxies in a given redshift bin for the construction of $\kappa_{\rm g}$. We predict this effect theoretically and find good agreement with the measurements, indicating that we can use this prediction to correct the bias obtained. The theoretical prediction describes the amplitude of the zero-lag correlations obtained using a given redshift bin for the foreground dark matter field, which by definition has a bias of 1. We can measure galaxy bias in that bin from the ratio between the zero-lag correlations of κ and $\kappa_{\rm g}$ (using the foreground galaxies in that bin) and the theoretical prediction as described in equations (26) and (27). This provides a useful tool to perform tomography and measure galaxy bias in single redshift bins. We measure and show the redshift-dependent bias obtained using this method for a flux-limited galaxy sample of $i < 22.5$ and find good agreement with the redshift-dependent bias from equation (3).

Other issues associated with observational data must be addressed if we apply this method to large galaxy surveys such as the Dark Energy Survey (DES). These issues include the conversion from $\kappa_{\rm g}$ to $\boldsymbol{\gamma}_{\rm g}$ or from $\boldsymbol{\gamma}$ to κ and its border effects, shape noise, masking, galaxy incompleteness, photo-z errors and boundary effects. As we measure fluctuations in the convergence maps, we are not affected by the mass-sheet degeneracy. We do not expect intrinsic alignments to affect our results, for several reasons. First, we use wide redshift binning for the cross-correlations between $\kappa_{\rm g}$ (or $\boldsymbol{\gamma}_{\rm g}$) and κ (or $\boldsymbol{\gamma}$) at different redshifts. Secondly, we never correlate lensing maps at different redshifts, so there is no Seljak & Hirata (2004) effect in our method. Finally, we could have intrinsic alignment effects from the correlations of lensing maps at the same redshift, so from $\langle\kappa\kappa\rangle$ or $\langle\boldsymbol{\gamma}\boldsymbol{\gamma}\rangle$. However, the estimators that optimize shape noise do not make use of these correlations, so the estimators that we want to use in observations, as applied in

Chang et al. (2016), do not present these contributions. We apply this method to the DES Science Verification data in a follow-up article (Chang et al. 2016). This method is expected to be significantly better when applied to larger areas, such as those in DES Year 1 (Diehl et al. 2014) or the 5000deg^2 from the expected total area of the DES survey, since the statistical errors will be smaller.

This article presents the method, but further studies can be carried out. We can explore galaxy bias for different galaxy samples, e.g. as a function of colour and luminosity. We expect different values of galaxy bias for different properties, since the clustering of galaxies depends on their properties (e.g. Zehavi et al. 2011). However, the accuracy of the method can also depend on the galaxy selection. First of all, the number density of galaxies has an impact on the precision of our estimation of the density field. Because of this, using a high threshold in colour or luminosity would imply a larger uncertainty in the measurement. Moreover, environmental dependences of galaxy bias might cause a stochasticity between galaxies and matter that might affect the bias estimation. This can happen for old and red galaxies, which are sensitive to the environment (Paranjape et al. 2015; Pujol et al. 2015). We can also explore the scale dependence of local bias by studying different angular scales and non-linearities and the redshift dependence by comparing tomographic measurements with the parametric redshift-dependent bias based on A12. In this article, we have focused on zero-lag cross-correlations, but we could also use two-point cross-correlations as a way to estimate the bias and include the redshift cross-correlations as a validation test.

The method studied in this article has several attractive features. First of all, the method is weakly dependent on cosmological parameters (it only depends strongly on $\Omega_{\rm m}$, as do many weak lensing measurements). It depends very weakly on σ_8 (only in non-linear corrections to f_1 and f_2), while other measurements of bias (from clustering statistics for example) are typically strongly dependent on σ_8 (Crocce et al. 2016; Giannantonio et al. 2016). This is because the ratios in the f_1 and f_2 factors cancel out most of the cosmology dependence. These factors include the 2PCF and geometric distances, which assume a flat Universe and geometry. Another advantage of the method is that it makes use of lensing maps to measure the matter distribution. Galaxy bias comes from a direct comparison between galaxy and matter distributions, while other methods usually compare the observed galaxy distribution with a simulated matter distribution. The method is also a good complement to other methods to measure galaxy bias from weak lensing, e.g. from galaxy–galaxy lensing or from cross-correlations between aperture mass and number counts. Apart from the fact that the cosmology dependences are different and hence a good complement, our method allows us to study local bias in the closest way to theory and *N*-body estimations. In that sense, our method is the most direct way to measure local bias with observations of both dark matter and galaxies.

This method is also similar to Hoekstra et al. (2002) and other measurements of bias from the cross-correlation between aperture mass and number counts. However, Hoekstra et al. (2002) look at small scales, where bias shows a significant scale dependence. In our case, we focus on large scales, where the bias is not scale-dependent and is consistent with linear bias. In fact, we have tested at what scales our measurement is consistent with linear bias and applied the method to these scales. Moreover, Hoekstra et al. (2002) uses the aperture mass statistics corresponding to a smoothing kernel of the matter field, which is different from the one we use here, and A12 showed that different smoothing schemes can produce different values of bias (due to the different contributions of the smallest scales). Our method allows the application of any smoothing scheme that might be useful for any particular study, although we use a boxcar smoothing that is easily comparable with the bias from *N*-body simulations and theory. Hence, using our method we can study both linear and non-linear bias by using large or small scales, although here we focus on linear scales.

A combined analysis of different measurements of galaxy bias, including this method, can be very useful to constrain bias and cosmology better. The method can also be applied to a situation where galaxies only cover partially the full redshift range of the lenses. Finally, the potential of this method will increase rapidly with data of present and upcoming surveys, such as the Hyper Suprime-Cam (HSC), the Dark Energy Survey (DES), the Kilo Degree Survey (KiDS), the Large Synoptics Survey Telescope (LSST), the Wide-Field Infrared Survey Telescope (WFIRST) and the *Euclid* mission.

ACKNOWLEDGEMENTS

We thank Juan Garcia-Bellido for the final revision of the article. The MICE simulations have been developed at the MareNostrum supercomputer (BSC-CNS) thanks to grants AECT-2006-2-0011 through AECT-2015-1-0013. Data products have been stored at the Port d'Informació Científica (PIC) and distributed through the CosmoHub webportal (cosmohub.pic.es). Funding for this project was partially provided by the Spanish Ministerio de Ciencia e Innovacion (MICINN), projects 200850I176, AYA2009-13936, AYA2012-39620, AYA2013-44327, ESP2013-48274, ESP2014-58384, Consolider-Ingenio CSD2007-00060, research project 2009-SGR-1398 from Generalitat de Catalunya and the Ramon y Cajal MICINN program. AP was supported by beca FI and 2009-SGR-1398 from Generalitat de Catalunya and project AYA2012-39620 from MICINN. CC, AA and AR are supported by the Swiss National Science Foundation grants 200021-149442 and 200021-143906. PF is funded by MINECO, project ESP2013-48274-C3-1-P.

REFERENCES

Amara A. et al., 2012, MNRAS, 424, 553 (A12)
Angulo R. E., Baugh C. M., Lacey C. G., 2008, MNRAS, 387, 921
Bartelmann M., Schneider P., 2001, Phys. Rep., 340, 291
Bel J., Hoffmann K., Gaztañaga E., 2015, MNRAS, 453, 259
Bernardeau F., 1996, A&A, 312, 11
Bernardeau F., Colombi S., Gaztañaga E., Scoccimarro R., 2002, Phys. Rep., 367, 1
Blanton M. R. et al., 2003, ApJ, 592, 819
Blanton M. R., Lupton R. H., Schlegel D. J., Strauss M. A., Brinkmann J., Fukugita M., Loveday J., 2005a, ApJ, 631, 208
Blanton M. R. et al., 2005b, AJ, 129, 2562
Buddendiek A. et al., 2016, MNRAS, 456, 3886
Cacciato M., Lahav O., van den Bosch F. C., Hoekstra H., Dekel A., 2012, MNRAS, 426, 566
Carretero J., Castander F. J., Gaztañaga E., Crocce M., Fosalba P., 2015, MNRAS, 447, 646
Chang C. et al., 2016, MNRAS, 459, 3203
Cole S., Kaiser N., 1989, MNRAS, 237, 1127
Coupon J. et al., 2012, A&A, 542, A5
Crocce M., Castander F. J., Gaztañaga E., Fosalba P., Carretero J., 2015, MNRAS, 453, 1513
Crocce M. et al., 2016, MNRAS, 455, 4301
Dark Energy Survey Collaboration, 2005, preprint (astro-ph/0510346)
Di Porto C. et al., 2014, preprint (arXiv:1406.6692)

Diehl H. T. et al., 2014, in Society of Photo-Optical Instrumentation Engineers (SPIE) Conference Series, Vol. 9149. SPIE, Bellingham, p. 0
Durkalec A. et al., 2015, A&A, 583, A128
Eisenstein D. J., Hu W., 1998, ApJ, 496, 605
Erben T. et al., 2013, MNRAS, 433, 2545
Eriksen M., Gaztañaga E., 2015, MNRAS, 452, 2168
Faltenbacher A., White S. D. M., 2010, ApJ, 708, 469
Flaugher B., 2005, Int. J. Mod. Phys. A, 20, 3121
Fosalba P., Gaztañaga E., Castander F. J., Manera M., 2008, MNRAS, 391, 435
Fosalba P., Crocce M., Gaztañaga E., Castander F. J., 2015a, MNRAS, 448, 2987
Fosalba P., Gaztañaga E., Castander F. J., Crocce M., 2015b, MNRAS, 447, 1319
Fry J. N., Gaztanaga E., 1993, ApJ, 413, 447
Gaztanaga E., Bernardeau F., 1998, A&A, 331, 829
Giannantonio T. et al., 2016, MNRAS, 456, 3213
Green J. et al., 2012, preprint (arXiv:1208.4012)
Heymans C. et al., 2012, MNRAS, 427, 146
Hildebrandt H. et al., 2016, preprint (arXiv:e-prints)
Hoekstra H., van Waerbeke L., Gladders M. D., Mellier Y., Yee H. K. C., 2002, ApJ, 577, 604
Hoffmann K., Bel J., Gaztañaga E., Crocce M., Fosalba P., Castander F. J., 2015, MNRAS, 447, 1724
Jullo E. et al., 2012, ApJ, 750, 37
Kaiser N., 1984, ApJ, 284, L9
Kaiser N., Squires G., 1993, ApJ, 404, 441
Kaiser N. et al., 2010, in Stepp L. M., Gilmozzi R., Hall H. J., eds, Society of Photo-Optical Instrumentation Engineers (SPIE) Conference Series, Vol. 7733. SPIE, Bellingham, p. 0
Kravtsov A. V., Klypin A. A., 1999, ApJ, 520, 437
Kuijken K. et al., 2015, MNRAS, 454, 3500
Laureijs R. et al., 2011, preprint (arXiv:1110.3193)
LSST Science Collaboration et al., 2009, preprint (arXiv:0912.0201)
Mandelbaum R., Slosar A., Baldauf T., Seljak U., Hirata C. M., Nakajima R., Reyes R., Smith R. E., 2013, MNRAS, 432, 1544
Manera M., Gaztañaga E., 2011, MNRAS, 415, 383
Manera M., Sheth R. K., Scoccimarro R., 2010, MNRAS, 402, 589
Marín F. A. et al., 2013, MNRAS, 432, 2654
Massey R. et al., 2007, Nat, 445, 286
Miyazaki S. et al., 2006, in McLean I. S., Iye M., eds, Society of Photo-Optical Instrumentation Engineers (SPIE) Conference Series, Vol. 6269. SPIE, Bellingham, p. 0
Mo H. J., White S. D. M., 1996, MNRAS, 282, 347
Paranjape A., Sefusatti E., Chan K. C., Desjacques V., Monaco P., Sheth R. K., 2013, MNRAS, 436, 449
Paranjape A., Kovač K., Hartley W. G., Pahwa I., 2015, MNRAS, 454, 3030
Pollack J. E., Smith R. E., Porciani C., 2014, MNRAS, 440, 555
Pujol A., Gaztañaga E., 2014, MNRAS, 442, 1930
Pujol A., Hoffmann K., Jiménez N., Gaztañaga E., 2015, preprint (arXiv:1510.01692)
Refregier A., 2003, ARA&A, 41, 645
Roth N., Porciani C., 2011, MNRAS, 415, 829
Schneider P., 1998, ApJ, 498, 43
Seljak U., Hirata C. M., 2004, Phys. Rev. D, 69, 043005
Seljak U., Warren M. S., 2004, MNRAS, 355, 129
Sheth R. K., Tormen G., 1999, MNRAS, 308, 119
Simon P., 2012, A&A, 543, A2
Simon P., Hetterscheidt M., Schirmer M., Erben T., Schneider P., Wolf C., Meisenheimer K., 2007, A&A, 461, 861
Smith R. E. et al., 2003, MNRAS, 341, 1311
Tinker J. L., Robertson B. E., Kravtsov A. V., Klypin A., Warren M. S., Yepes G., Gottlöber S., 2010, ApJ, 724, 878
van Waerbeke L., 1998, A&A, 334, 1
Van Waerbeke L. et al., 2013, MNRAS, 433, 3373
Vikram V. et al., 2015, Phys. Rev. D, 92, 022006
White S. D. M., Rees M. J., 1978, MNRAS, 183, 341
Zehavi I. et al., 2011, ApJ, 736, 59
Zentner A. R., Hearin A. P., van den Bosch F. C., 2014, MNRAS, 443, 3044

This paper has been typeset from a TEX/LATEX file prepared by the author.